Physica E 122 (2020) 114157

Contents lists available at ScienceDirect

Physica E: Low-dimensional Systems and Nanostructures

journal homepage: www.elsevier.com/locate/physe

Pristine and strained anisotropic group velocity and effective mass of surface Dirac fermions in the topological crystalline insulator SnTe

Nguyen T.T. Binh [a], Bui D. Hoi [b], Ho Viet [c], Tong S. Tien [d], Pham V. Dung [e], Nguyen T. Dung [f], P.T.T. Le [g,h,*]

[a] Institute of Research and Development, Duy Tan University, 03 Quang Trung, Danang, Viet Nam
[b] Department of Physics, University of Education, Hue University, 34 Le Loi, Hue City, Viet Nam
[c] Department of Research Management and International Relations, Hue Industrial College, Hue City, Viet Nam
[d] Department of Basic Science, University of Fire Fighting and Prevention, No. 243, Khuat Duy Tien, Thanh Xuan Dist., Ha Noi, Viet Nam
[e] Nguyen Hue University, Dong Nai Province, Viet Nam
[f] Vinh University, Nghe An Province, Viet Nam
[g] Laboratory of Magnetism and Magnetic Materials, Advanced Institute of Materials Science, Ton Duc Thang University, Ho Chi Minh City, Viet Nam
[h] Faculty of Applied Sciences, Ton Duc Thang University, Ho Chi Minh City, Viet Nam

ABSTRACT

An analysis of the strain-induced group velocity (GV) and effective mass (EM) of massless topological Dirac fermions on the SnTe (001) surface, protected by crystalline symmetry, is presented. Using the traditional semi-classical $\vec{k} \cdot \vec{p}$ approach by associating fermions with wave-packets, we find that the expression for the energy dispersion surface as well as both GV and EM are anisotropic in the absence and presence of strain. The band structure calculations indicate that the massive Dirac fermions emerge for strained SnTe (001) surface. However, under strong strains, GVs and EMs of all branches of conduction and valence bands are the same quantitatively, but still anisotropic along different directions. On the other hand, depending on the special critical compressive and/or tensile strains, the direction of the fermionic waves is reversed. Further, the behavior of heavy and light masses are characterized qualitatively with strain modulus and direction. Our results are favorable for the thermoelectric properties of SnTe semiconductor since electronic features are coupled to the heat transports.

1. Introduction

The "non-trivial" band structure including gapless states in HgTe quantum well [1,2] opened a new window for finding gapless critical phases in novel quantum materials both theoretically and experimentally in both two-dimensional (2D) and three-dimensional (3D) [3–12]. Previously, the researchers were dealing with the gapless states in 2D materials such as graphene [pristine state], silicene and related group-IV materials [in the presence of electric field equal to the intrinsic spin–orbit coupling], etc. [13–24]. Topological insulator (TI) is a name for such novel quantum systems characterized by topological invariants such as $\mathbb{Z}_2$ time-reversal symmetry, particle–hole symmetry, chiral symmetry, and a gapped bulk state [3–6,25,26]. An insulating bulk and metallic surface states come into play role in determining novel topological features in TIs [27–29]. However, it has been demonstrated that the topological classification of band structures is not restricted to these symmetries only and "spatial symmetries" indicate topological phases as well [30–32,28,27].

Theoretically, a new class of topological band structures, so-called topological crystalline insulators (TCIs) [27,30,33], has been predicted considering the crystal point-group symmetries such as mirror, rotation or glide. The first experimentally realization of TCIs belong to the lead thin salt family in IV–VI semiconductors, SnTe, $Pb_{1-x}Sn_xSe$ ($x \geq 0.2$) and $Pb_{1-x}Sn_xTe$ ($x \geq 0.4$) [30–32]. The non-trivial topology of electronic bands in TCIs originates from the reflection symmetry with respect to the (110) mirror plane [30–32,28,34]. In TCIs, there are two types of metallic gapless states, which depend strongly on the crystal face orientation. First one is the (111) surface state (four Dirac cones centered at time-reversal-invariant Γ and M points) for which L_1 ($\{L_2, L_3, L_4\}$) point of bulk Brillouin zone of rock salt lattice is projected to Γ (M) point of the surface Brillouin zone, while for the second {(110),(001)} surface states the $\{L_1, L_2\}$ ($\{L_3, L_4\}$) points of bulk Brillouin zone are projected to X_1 (X_2) and X (R) point of surface Brillouin zone in the (001) and (110) plane, respectively [35]. In the case of (001) surface states, four Dirac cones centered at non-time-reversal-invariant X_1 and X_2 points are included [35,31,32,28,36,37] and demonstrate robust surface states in TCI SnTe and related alloys [35,38–48]. This is one of the reasons why we will focus on such a surface in the present work.

* Corresponding author at: Laboratory of Magnetism and Magnetic Materials, Advanced Institute of Materials Science, Ton Duc Thang University, Ho Chi Minh City, Viet Nam.
E-mail address: lethithuphuong@tdtu.edu.vn (P.T.T. Le).

https://doi.org/10.1016/j.physe.2020.114157
Received 5 January 2020; Received in revised form 10 March 2020; Accepted 23 April 2020
Available online 27 April 2020

In contrast to robust TI surface states, the electronic features of TCI materials can be easily tuned with external perturbations [33], changing in the topological invariants [49,50,30,51–56]. A mechanical strain leads to a shift in the Dirac point positions and eventually the band gap opening [52,53,57]. This, in turn, implies that the physical features of the system can be controlled. In addition to the mechanical perturbations, in Ref. [58], the Dirac mass generation using a magnetic dopant breaks down the time-reversal-symmetry and a Zeeman gap opens at four Dirac points of (001) surface, offering a large quantized Hall conductance [30,59]. Or, a perpendicular electric field opens up gap energy [54], introducing a topological transistor with tunable ON and OFF states. Thus, TCIs based on IV–VI semiconductors are extremely versatile platforms for novel device applications, however; the investigation of fundamental physical properties of perturbed gapless Dirac fermions in such systems is still of great interest.

In this paper, we adopt the strain effects stemming from the compressive and tensile strains to study the group velocity and effective mass of Dirac fermions on the SnTe (001) surface. It has been shown that the structural distortion from a relative displacement of the cation and anion sublattices in IV–VI semiconductors leads to a net ferroelectric polarization and eventually massive Dirac fermions on (001) surface [30,60]. Since both the electronic properties of semiconductors and thermoelectrics, in particular, are typically understood using band models, transport is then understood in terms of band expressions with a varying group velocity and effective mass. To the best of our knowledge, such a study has not yet been reported to date and it is the first time to do so theoretically. We add the strain-induced momenta term to the effective $\vec{k}\cdot\vec{p}$ model to get into the goal.

The paper is organized as follows. In Section 2, we briefly review the effective $\vec{k}\cdot\vec{p}$ Hamiltonian model of SnTe (001) surface states, which is strongly needed to address the iso-energy and electronic band structures along different high-symmetry points in the surface Brillouin zone (SBZ). Also, the "pristine" group velocity (GV) and effective mass (EM) calculations are included in this section. In Section 3, we present and discuss manipulated GV and EM by the above-mentioned strain effects. To do so, the traditional semi-classical approach by associating particles with wave-packets is used for calculations of the fermionic transport properties. The paper ends in Section 4.

2. Theory and method

In this section, the basic theoretical background of the SnTe (001) surface Dirac fermions, as well as related alloys, is presented. We set the physical constant $\hbar = 1$ for simplicity throughout the paper. To confirm the experimental observations for the band structure of the SnTe (001) surface states, the following "clean" $\vec{k}\cdot\vec{p}$ Hamiltonian near both X_1 and X_2 points of the SBZ is proposed [31,32,28]:

$$\hat{\mathcal{H}}_{X_1}(\vec{k}) = \eta_x k_x \hat{\sigma}_y - \eta_y k_y \hat{\sigma}_x + n\hat{\tau}_x + \delta\hat{\sigma}_y\hat{\tau}_y\,, \tag{1a}$$

$$\hat{\mathcal{H}}_{X_2}(\vec{k}) = \eta_y k_x \hat{\sigma}_y - \eta_x k_y \hat{\sigma}_x + n\hat{\tau}_x + \delta\hat{\sigma}_x\hat{\tau}_y\,, \tag{1b}$$

where $\eta_x = 1.3$ eV Å and $\eta_y = 2.4$ eV Å are typical values obtained from numerical *ab initio* computations [30,35,60]. While $\hat{\vec{\sigma}} = (\hat{\sigma}_x, \hat{\sigma}_y)$ are the Pauli matrices for two spin components, so-called Kramer's doublet, the Pauli matrices for the pseudospin describing the cation–anion degree of freedom are given by $\hat{\vec{\tau}} = (\hat{\tau}_x, \hat{\tau}_y)$. As for the intervalley scattering at the lattice scale, two parameters $n = 70$ meV and $\delta = 26$ meV are introduced having only three allowed symmetry operators $\hat{\tau}_x$, $\hat{\sigma}_x\hat{\tau}_y$ and $\hat{\sigma}_y\hat{\tau}_y$ up to zeroth order momenta $\vec{k} = (k_x, k_y)$ [30].

From Eqs. (1a) and (1b), the transformation of $\hat{\mathcal{H}}_{X_1}(\vec{k}) \Leftrightarrow \hat{\mathcal{H}}_{X_2}(\vec{k})$ is evident due to four-fold C_4 discrete rotation symmetry described by $\hat{\sigma}_x \mapsto \hat{\sigma}_y$, $\hat{\sigma}_y \mapsto -\hat{\sigma}_x$, $k_x \mapsto k_y$, and $k_y \mapsto -k_x$. From this point, we will focus on the dynamics near one of the X_1 and X_2 points in what follows. Thus, simply, the matrix form of Eq. (1a) can be written as

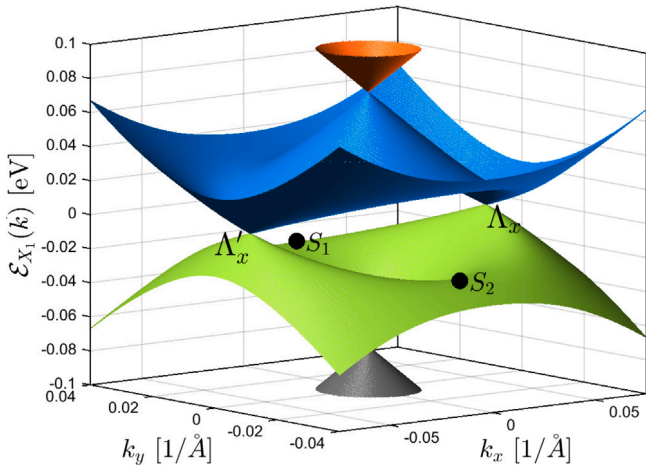

Fig. 1. Three-dimensional electronic dispersion energy of Dirac fermions on the SnTe (001) surface near the X_1 point of the SBZ. Two saddle points contribute to the carrier dynamics with the coordinates $S_1 = (0, +n/\eta_y)$ and $S_2 = (0, -n/\eta_y)$. Also, the Dirac cones at $\vec{k} = 0$ are located at energies $\mathcal{E} = \pm\sqrt{n^2+\delta^2}$, while two Dirac cones at $\mathcal{E} = 0$ have the wave-vector coordinates $\Lambda_x = (+\sqrt{n^2+\delta^2}/\eta_x, 0)$ and $\Lambda'_x = (-\sqrt{n^2+\delta^2}/\eta_x, 0)$. (For interpretation of the references to color in this figure legend, the reader is referred to the web version of this article.)

$$\underline{\underline{\mathcal{H}}}_{X_1}(\vec{k}) = \begin{pmatrix} 0 & n & f(\vec{k}) & -\delta \\ n & 0 & \delta & f(\vec{k}) \\ f^*(\vec{k}) & \delta & 0 & n \\ -\delta & f^*(\vec{k}) & n & 0 \end{pmatrix}, \tag{2}$$

in which $f(\vec{k}) = -\mathrm{i}\eta_x k_x - \eta_y k_y$. The Dirac energy–momentum dispersions for four gapless states above-mentioned can be easily obtained via diagonalizing the above Hamiltonian, given by

$$\mathcal{E}^{\mu,\nu}_{X_1}(\vec{k}) = \mu\sqrt{g(\vec{k}) + \nu h(\vec{k})}\,, \tag{3a}$$

$$g(\vec{k}) = n^2 + \delta^2 + \eta_1^2 k_x^2 + \eta_2^2 k_y^2\,, \tag{3b}$$

$$h(\vec{k}) = 2\sqrt{(n^2+\delta^2)\eta_1^2 k_x^2 + n^2\eta_2^2 k_y^2}\,, \tag{3c}$$

where $\mu = +(-)$ and $\nu = +(-)$ stand for the conduction (valence) band and Λ_x (Λ'_x) point, respectively [see Fig. 1]. From this equation, one obtains various information about the direction-dependent dispersing. At $\vec{k} = 0$, energies $\mathcal{E} = \pm\sqrt{n^2+\delta^2}$ and at $\mathcal{E} = 0$, the momenta $\Lambda_x = (+\sqrt{n^2+\delta^2}/\eta_x, 0)$ and $\Lambda'_x = (-\sqrt{n^2+\delta^2}/\eta_x, 0)$ at $k_y = 0$, referring to the metallic gapless SnTe (001) surface states, are obtained. In addition, at $k_x = 0$, one achieves two saddle points $S_1 = (0, +n/\eta_y)$ and $S_2 = (0, -n/\eta_y)$ along the y direction. At these saddle points, two disconnected electron packets at low-energy Dirac cones suffer from a Lifshitz transition at energy $\mathcal{E} = \pm\delta = \pm 26$ meV.

It should be mentioned that in Fig. 1, the lowest valence band is the gray band, the highest valence band is the green band, the lowest conduction band is the blue band, and the highest conduction band is the red band. These colors are the characterizations for the following curves of both GV and EM plots. However, we restrict ourselves to the conduction bands only, since there exists electron–hole symmetry between valence and conduction bands. For this reason, blue and red ones are illustrated in Figs. 2–5. Let us focus on "clean" GV and EM of Dirac fermions on the SnTe (001) surface.

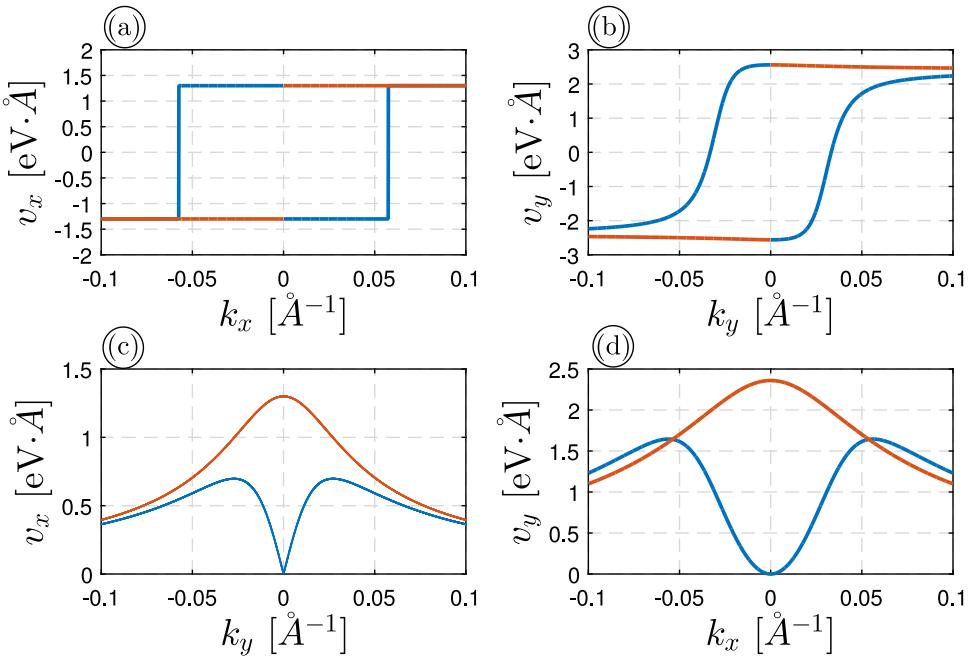

Fig. 2. Direction-dependent group velocity of Dirac fermions on the SnTe (001) surface for (a) $k_y = 0$, (b) $k_x = 0$, (c) $k_x = +\sqrt{n^2+\delta^2}/\eta_x$, and (d) $k_y = +n/\eta_y$. (For interpretation of the references to color in this figure legend, the reader is referred to the web version of this article.)

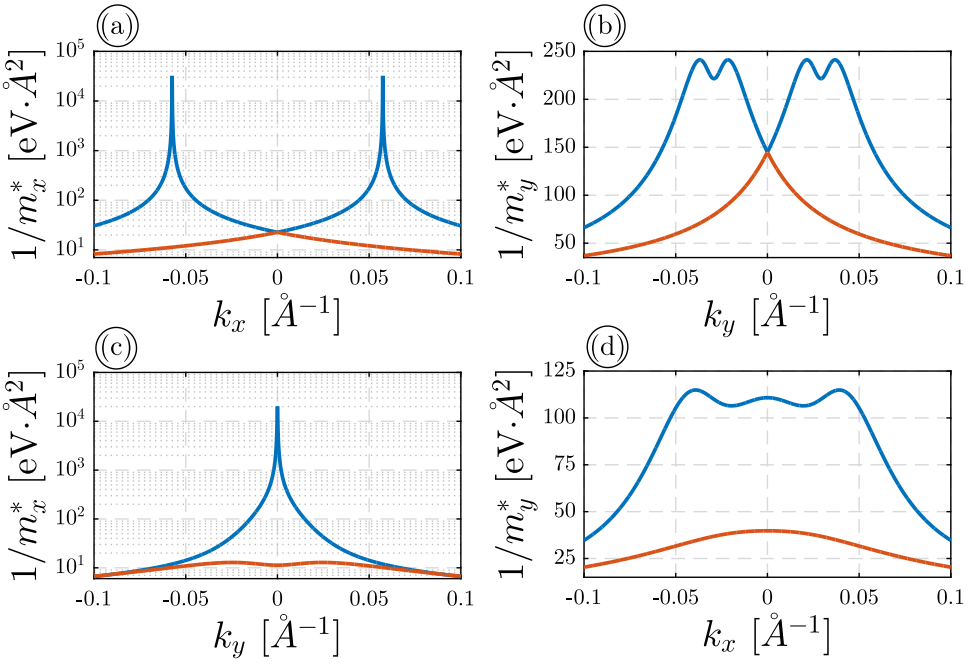

Fig. 3. Direction-dependent effective mass of Dirac fermions on the SnTe (001) surface for (a) $k_y = 0$, (b) $k_x = 0$, (c) $k_x = +\sqrt{n^2+\delta^2}/\eta_x$, and (d) $k_y = +n/\eta_y$. (For interpretation of the references to color in this figure legend, the reader is referred to the web version of this article.)

2.1. Pristine group velocity of Dirac fermions on the SnTe (001) surface

As well-known, the basic properties of electron transport phenomena in a solid crystal lattice are described in terms of Bloch electronic waves with wave vectors $\vec{k}$ [61,62]. The $\vec{k}$-dependent GV is the certain velocity of built dispersive wave packet from these Bloch waves, which for the flavor $\alpha \in \{x, y\}$ can be shown quite generally that

$$v_\alpha^{\mu,\nu}(\vec{k}) = \partial_{k_\alpha} \mathcal{E}_{X_1}^{\mu,\nu}(\vec{k}). \tag{4}$$

This equation gives rise to the real-space motion of the fermions. As mentioned before, here we have $\mu = +$ and $\nu = \pm$ only and the results for $\mu = -$ are the same with a different sign. Thus, by substituting Eq. (3a) into Eq. (4) we obtain

$$v_x^{\mu,\nu}(\vec{k}) = \frac{\eta_1^2 k_x}{\mathcal{E}_X^{\mu,\nu}(\vec{k})}\left(1 + 2\nu\frac{n^2+\delta^2}{g(\vec{k})}\right), \tag{5a}$$

$$v_y^{\mu,\nu}(\vec{k}) = \frac{\eta_2^2 k_y}{\mathcal{E}_X^{\mu,\nu}(\vec{k})}\left(1 + 2\nu\frac{n^2}{g(\vec{k})}\right). \tag{5b}$$

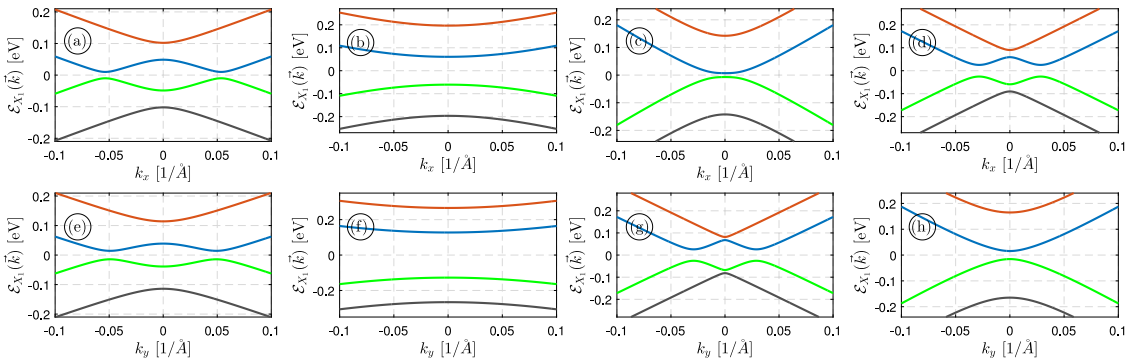

Fig. 4. Strained two-dimensional electronic dispersion energy of Dirac fermions on the SnTe (001) surface near the X_1 point of the SBZ for (a) $\{k_y = 0, u_{xx} = 0, u_{yy} = \pm 0.04\}$, (b) $\{k_y = 0, u_{xx} = \pm 0.04, u_{yy} = 0\}$, (c) $\{k_y = +n/\eta_y, u_{xx} = 0, u_{yy} = \pm 0.04\}$, (d) $\{k_y = +n/\eta_y, u_{xx} = \pm 0.04, u_{yy} = 0\}$, (e) $\{k_x = 0, u_{xx} = 0, u_{yy} = \pm 0.04\}$, (f) $\{k_x = 0, u_{xx} = \pm 0.04, u_{yy} = 0\}$, (g) $\{k_x = +\sqrt{n^2+\delta^2}/\eta_x, u_{xx} = 0, u_{yy} = \pm 0.04\}$, (h) $\{k_x = +\sqrt{n^2+\delta^2}/\eta_x, u_{xx} = \pm 0.04, u_{yy} = 0\}$. (For interpretation of the references to color in this figure legend, the reader is referred to the web version of this article.)

Of course, the GV norm can be also calculated using $|v^{\mu,\nu}(\vec{k})| = \sqrt{[v_x^{\mu,\nu}(\vec{k})]^2 + [v_y^{\mu,\nu}(\vec{k})]^2}$, however; we are interested in details of components in the absence and presence of external strain perturbation. This helps us to confirm our claim on the anisotropic properties of SnTe (001) surface.

In Fig. 2, we plot the orientation-dependent GV of Dirac fermions for pure SnTe (001) surface. Using Fig. 1, we have set four cases for the velocities including $k_y = 0$, $k_x = 0$, $k_x = \sqrt{n^2+\delta^2}/\eta_x$, and $k_y = n/\eta_y$, as shown in Fig. 2. For first two cases, we purely are along the x and y direction, respectively, while in second two cases the critical momenta at saddle point A_x and S_1 are chosen, supporting the role of intervalley scattering parameters n and δ. For $k_y = 0$, we have the GV

$$v_x^{\nu}(k_x) = \frac{\eta_x}{\mathcal{E}_X^{\nu}(k_x, 0)} \left(\eta_x k_x + \nu\sqrt{n^2+\delta^2}\right),$$

leading to the panel (a) in Fig. 2. It is clear that at $v_x = \pm\eta_x$, the Dirac fermions behave linearly with k_x and at $k_x = \pm\sqrt{n^2+\delta^2}/\eta_x$, it is zero. That can be understood from the slope of bands in Fig. 1 as well. For the case of $k_x = 0$, i.e. Fig. 2(b), we obtain

$$v_y^{\nu}(k_y) = \frac{\eta_y}{\mathcal{E}_X^{\nu}(k_y, 0)} \left(\eta_y k_y + \nu n\right).$$

The GV of upper band of the conduction band (red band) shows almost a plateau with the value of $v_y = \eta_y$, implying that at $k_x = 0$ Dirac fermions propagate independent of the k_y momentum, while the lower band of the conduction band (blue band) shows an increasing behavior with $\pm k_y$.

As for the case of $k_x = \sqrt{n^2+\delta^2}/\eta_x$, the GV versus k_y indicates a symmetric plot with respect to the k_y, as illustrated in Fig. 2(c). This stems from the mirror symmetry of the dispersing branches of the band structure. To avoid confusion with many equations, the analytical relations are not presented anymore. At $k_y = 0$, while v_x is zero for blue conduction band, it is maximum (η_x) for the red conduction band. In addition, there are two extremum k_y-points for which the GV along x-direction is maximized to $\eta_x/2$ and those points are exactly equal to the saddle points $|n/\eta_y|$. The last case, Fig. 2(d), shows v_y versus k_x when the momentum along the y-direction is fixed at $k_y = n/\eta_y$. The same behavior as Fig. 2(c) can be seen. The maximum value of v_y at $k_x = 0$ is η_y for the lowest conduction band, while at the Dirac points $|\sqrt{n^2+\delta^2}/\eta_x|$, the maximum value of around 1.6 is obtained.

It is important to note that at low momenta, in the vicinity of Dirac points $k_x = k_y = 0$, near $k_x \neq 0$ and $k_y = 0$ as well as near $k_y \neq 0$ and $k_x = 0$, v_x and v_y are isotropic for all bands, coinciding with the η_x and η_y, respectively. However, as we add strain corrections to the Dirac cones (moving away from the Dirac points), they are anisotropic. In general, a strong anisotropic feature is seen for v_x and v_y themselves. From these results, it is obvious that strain corrections and directions should be considered in the calculations of physical quantities, since perturbation effects enhance these features, as we discuss in the next section. As a quick comparison with the Dirac cones in graphene and other 2D systems, one stress that these results do not appear when the Dirac theory is used only. By this, we mean that in the absence of intervalley scattering parameters n and δ, the same behaviors (but doubled) appear for SnTe (001) surface Dirac fermions. Let us turn to another fundamental electronic transport property, EM.

2.2. Pristine effective mass of Dirac fermions on the SnTe (001) surface

In theoretical physics, the concept of mass has a long history and there are many different EM definitions [63–66]. To motivate the reader about the EM calculations, it is worth noting that EM treatment gives rise to an in-depth understanding of the fundamental electro-optical properties, which is yet to be established for the design and development of functional SnTe (001) surface-based devices. In doing so, it is common to use an alternative definition, i.e. the second derivative of the energy dispersion, which is generally energy and momentum dependent. It should be noted that this definition is sometimes referred to as the optical EM [64]. So, for the flavor $\alpha \in \{x, y\}$, the EM can be calculated straightforwardly

$$\frac{1}{m_{\alpha}^{*\mu,\nu}(\vec{k})} = \partial_{k_\alpha}^2 \mathcal{E}_{X_1}^{\mu,\nu}(\vec{k}). \tag{6}$$

Simply, the following expressions are derived using the implicit second derivative of the Eq. (3a)

$$\frac{1}{m_x^{*\mu,\nu}(\vec{k})} = -\frac{\eta_1^4 k_x^2}{\left[\mathcal{E}_X^{\mu,\nu}(\vec{k})\right]^3}\left(1 - 2\nu\frac{n^2+\delta^2}{g(\vec{k})}\right)^2 - \frac{\eta_1^2}{\mathcal{E}_X^{\mu,\nu}(\vec{k})}\left(1 + 8\nu\frac{\eta_1^2 k_x^2 \left(n^2+\delta^2\right)^2}{g^3(\vec{k})} - 2\nu\frac{n^2+\delta^2}{g(\vec{k})}\right), \tag{7a}$$

$$\frac{1}{m_y^{*\mu,\nu}(\vec{k})} = -\frac{\eta_2^4 k_y^2}{\left[\mathcal{E}_X^{\mu,\nu}(\vec{k})\right]^3}\left(1 - 2\nu\frac{n^2}{g(\vec{k})}\right)^2 - \frac{\eta_2^2}{\mathcal{E}_X^{\mu,\nu}(\vec{k})}\left(1 + 8\nu\frac{\eta_2^2 k_y^2 n^2}{g^3(\vec{k})} - 2\nu\frac{n^2}{g(\vec{k})}\right). \tag{7b}$$

Generally, an increase or decrease of the EM with wave-vector or even the external physical perturbations is related to those density of states that is larger or smaller than that of the principal one. This implies that the concavity of energy bands is directly concentrated on the degeneracy of those bands, characterizing the density of states. From Fig. 1, it would seem that the energy separation between band edges along the y-direction is considerably greater compared to the x-direction, and the principal band edge effective mass along x-direction

is much smaller than the y-direction. This is confirmed in Fig. 3 for which $1/m_x^* > 1/m_y^*$ or $m_x^* < m_y^*$ independent of the momenta. This, in turn, means that the state associated with the heavy-mass band is related to the y-direction and the transport is faster along the x-direction.

Our plotted results in Fig. 3 (a), (b), (c), and (d) are, respectively, shown for four typical wave-vectors $k_y = 0$, $k_x = 0$, $k_x = +\sqrt{n^2+\delta^2}/\eta_x$, and $k_y = +n/\eta_y$. Similar to the GV, for $k_x = k_y = 0$ values, the EM of both conduction bands are isotopic, while when one of them is zero only, there is an anisotropic so that EM is maximum for the lowest conduction band (blue band) and it is minimum for the highest conduction band (red band). Again, the maximum value of EM in panel (a), i.e. when $k_y = 0$, is taken place at $k_x = \pm\sqrt{n^2+\delta^2}/\eta_x$, whilst it is (on average) the case at $k_y = \pm n/\eta_y$ for EM in panel (b). Due to the concavity of the bands at these critical momenta, a minimum and maximum EM was expected clearly, as confirmed by the inverse of EMs in panels (a) and (b). That is also the case in panels (c) and (d) for which the concavity is small and large, respectively, leading to the minimum and maximum EM. To ensure a fair comparison with the specific momenta examined here, we are also able to calculate the EM over the whole SBZ, however, the corresponding results are not presented here and need to be investigated in another way.

3. Strain effects

In this section, we apply the strain theory to evaluate the nature of the impact of the theory on electronic band structure as well as on both GV and EM of Dirac fermions on the SnTe (001) surface. Considering the strain modulus in the band model, we derive a tractable expression for the bands and their GV and EM. We wish to make it clear that while the theory considers the shift in momenta and energy, the electronic transport properties are enhanced significantly.

The strain is one of the effective ways of moving the mirror symmetry protected Dirac points of SnTe (001) surface, leading to the so-called crystal mirror symmetry breaking phenomenon. It is noteworthy to mention that the real-space wave functions corresponding to the bands become compressed and tensioned in the presence of compressive and tensile strain, respectively, leading to bonding and non-bonding states. These quantum effects manifest themselves in transport and accordingly GV and EM as well. In the presence of strain, it is simple to state that the Dirac points surface suffer from a displacement $\vec{u}$ with components $u_{ij} = (\partial_j u_i + \partial_i u_j)/2$, which can be addressed by a strain-induced gauge field vector potential $\vec{A} = \bar{\vec{A}}_x - \vec{A}_x$, where $\bar{\vec{A}}_x$ are the momenta in the presence of strain. The linear relationship between the spatial displacement $\vec{u}$ and $\vec{A}$ is given by [53,67,68]

$$\vec{A} = (\alpha_1 u_{xx} + \alpha_2 u_{yy}, \alpha_1 u_{yy} + \alpha_2 u_{xx}), \tag{8}$$

where $\alpha_{\{1,2\}}$ are the independent coupling constants. Note that the shear terms $\{u_{xy}, u_{yx}\}$ are neglected for simplicity. As for the non-linear terms, there is no explicit analytical expression yet and to have a stable system, it can be neglected simply. By this, the shift in the momenta can be written as

$$k_x \longmapsto k_x + \alpha_1 u_{xx} + \alpha_2 u_{yy}, \tag{9a}$$

$$k_y \longmapsto k_y + \alpha_1 u_{yy} + \alpha_2 u_{xx}. \tag{9b}$$

for $\alpha_1 = 0.3$ Å^{-1} and $\alpha_2 = 1.4$ Å^{-1} [69]. Although we restrict ourselves to the X_1 point, the statements are similar for the X_2 point applying the transformations mentioned above the Eq. (2). We label the tensile and compressive strains with the signs + and −, respectively. Depending on the strain modulus u_{xx} and u_{yy}, the dispersion energy of the system is illustrated in Fig. 4 for two arbitrary strains ±0.04 and different momenta configurations. There is no physical reason for such a strain modulus and it can be examined with other strengths as well. While there is an advantage in the made approximation in its easiness to work with, there is also a disadvantage in the sense it is not exact in some sense and its region of validity if any is unclear. However, we leave further investigations for our future research to come.

As can be seen from Fig. 4(a) and (b) with $\{k_y = 0, u_{xx} = 0, u_{yy} = \pm 0.04\}$ and $\{k_y = 0, u_{xx} = \pm 0.04, u_{yy} = 0\}$, respectively, while the system is gapped in the presence of both u_{xx} and u_{yy}, the electronic transport properties are anisotropic with respect to the strain direction. The variation of the gaps in both $k_x = 0$ and $k_x = \pm\sqrt{n^2+\delta^2}/\eta_x$ is exactly the variation of Dirac points, which clearly alters the GV and EM quantities. However, if we consider a non-zero momentum along the y-direction, we have Fig. 4(c) and (d) with $\{k_y = +n/\eta_y, u_{xx} = 0, u_{yy} = \pm 0.04\}$ and $\{k_y = +n/\eta_y, u_{xx} = \pm 0.04, u_{yy} = 0\}$, respectively. At first glance, parabolic dispersions emerge for the u_{yy}, while the same behavior as the case of $k_x = 0$ and $u_{xx} = 0$ appears for the u_{xx} and the gaps for both time-reversal and mirror symmetry points are increased with the presence of non-zero k_y. Shortly, the Dirac cones at zero energy change less than those with non-zero energies $\pm\sqrt{n^2+\delta^2}$, implying that the strain-tuned intervalley δ parameter is more than important in the formation of TCI phase as well as in the topological phase transitions.

The anisotropic result along different directions shown in Fig. 1 alerts to consider the same behaviors for the band structure versus k_y. In Fig. 4(e)–(h), we anticipate some results for $\mathcal{E}_{X_1}(\vec{k})$ in terms of k_y when uniaxial strains along both directions are applied in the case of zero and non-zero k_x as (e) $\{k_x = 0, u_{xx} = 0, u_{yy} = \pm 0.04\}$, (f) $\{k_x = 0, u_{xx} = \pm 0.04, u_{yy} = 0\}$, (g) $\{k_x = +\sqrt{n^2+\delta^2}/\eta_x, u_{xx} = 0, u_{yy} = \pm 0.04\}$, and (h) $\{k_x = +\sqrt{n^2+\delta^2}/\eta_x, u_{xx} = \pm 0.04, u_{yy} = 0\}$. From Fig. 1, one sees that at $k_x = k_y = 0$, the band dispersion possesses two Dirac cones with non-zero energies only. On the other hand, Fig. 4(e) and (f) show that while those Dirac cones are gapped when u_{yy} or u_{xx} is turned on, the band gap opening process is anisotropic for the case of u_{xx} and/or u_{yy}. This implies that in the case of $u_{xx} = \pm 0.04$, purely parabolic curves appear, whilst this is not the case for $u_{yy} = \pm 0.04$. Furthermore, it is clear from Fig. 4(g) and (h) that the Dirac points at X_1 point gets anticrossed phase faster, if one applies the strain along the x edge, than the y edge independent of the strain sign. Moreover, the parabolic-shape curve holds with strain similar to the panel (c). The results are in agreement with Refs. [52,55,49,67,68].

Let us focus on the main goal of the present paper, i.e. strain-induced GV and EM of surface Dirac fermions on the SnTe(001). Unless noted otherwise we take $-10\% \leq u_{xx/yy} \leq +10\%$ to avoid misjudging situations where no isotropic behavior occurs later. We analyze the particular cases of pure uniaxial strains along the x- and y-direction, as shown in Figs. 5 and 6. To validate the following results, we stress that the band structure changes under strain are only needed for understanding and confirming the GV and EM results. Since in the previous parts, we confirmed that the results are correct and valid, the GV and EM results must be valid as well because they are the counterparts of the band structure and all the changes made in the band structure manifest itself in the GV and EM automatically.

It can be observed from Fig. 5(a) that in the directions where the compressive strains appear, v_x independent of the conduction bands is negative and increases slightly with u_{xx} at $u_{yy} = -0.04$. The negative sign of GV means that the direction of spatial wave-function propagation is along the $-x$-direction. In tensile strains, however, v_x of the lowest (highest) conduction band increases (decreases) drastically with positive (negative) sign. Finally, at $u_{xx} = k_x = +\sqrt{n^2+\delta^2}/\eta_x$, both GVs of conduction bands converge to a positive sign. It seems that the net electronic wave-functions propagate along the $+x$-direction for $u_{xx} > +\sqrt{n^2+\delta^2}/\eta_x$. Also, v_x is no longer isotropic with respect to the u_{xx}. For Fig. 5(b), which describes the GV v_x versus u_{yy} at the same k_x as panel (a) and $u_{xx} = +0.04$, the effects caused by the deformation in the wave-function surfaces are increasing trends for both compressive and tensile strains. Interestingly, there is a direction switching for the orientation of propagation at the critical $u_{yy} = -k_x$ with a zero value for v_x, while both GVs of conduction bands converge again to the positive

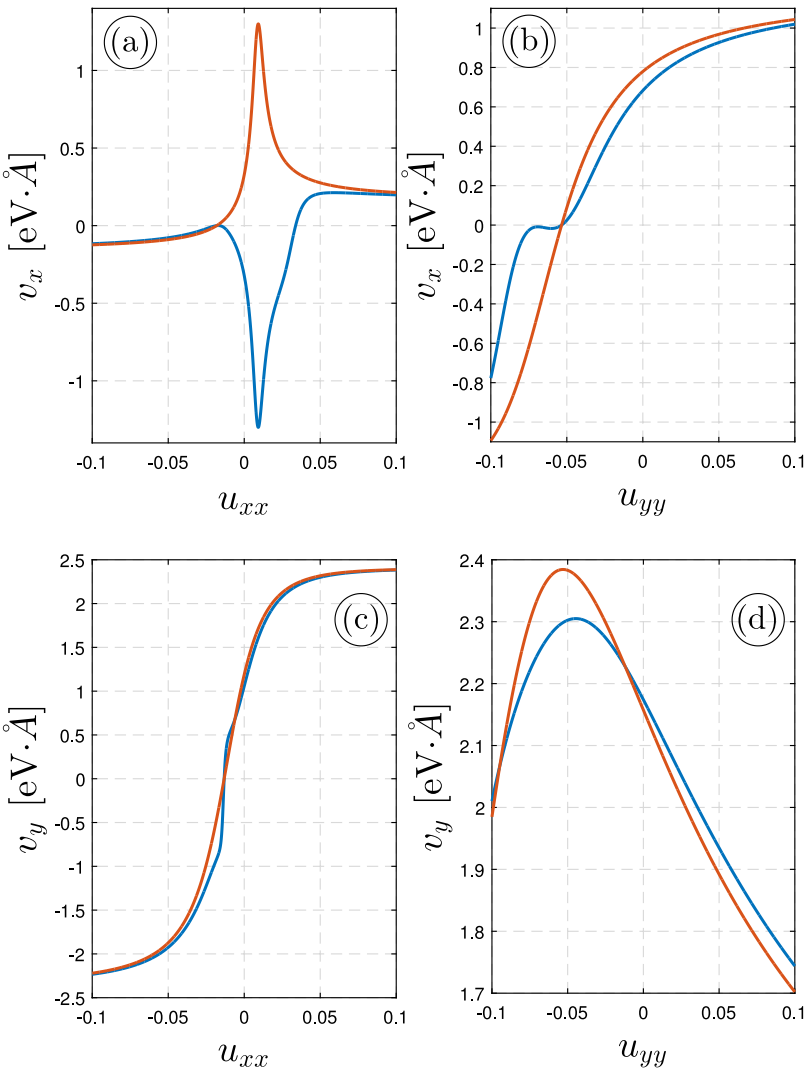

Fig. 5. Direction-dependent group velocity of Dirac fermions on the SnTe (001) surface for (a) $\{k_y = 0, k_x = +\sqrt{n^2+\delta^2}/\eta_x, u_{yy} = -0.04\}$, (b) $\{k_y = 0, k_x = +\sqrt{n^2+\delta^2}/\eta_x, u_{xx} = +0.04\}$ $k_x = 0$, (c) $\{k_x = 0, k_y = +n/\eta_y, u_{yy} = -0.04\}$, and (d) $\{k_x = 0, k_y = +n/\eta_y, u_{xx} = +0.04\}$. (For interpretation of the references to color in this figure legend, the reader is referred to the web version of this article.)

values and propagate along the $+x$-direction. It should be mentioned that the maximum and converged values of v_x in the above-mentioned cases are the value of η_x.

Plots of the GV v_y along the y-direction for a uniaxial uniform strain given by u_{xx} and u_{yy} at $k_y = +n/\eta_y$ are shown in Fig. 5(c) and (d), respectively. The increase of v_y with u_{xx} is visible for both conduction bands and it gets zero at a critical compressive strain $u_{xx} = -0.02$. Moreover, although both bands behave similarly with u_{xx} at $u_{yy} = -0.04$, it becomes anisotropic again beside the direction switching of propagation caused by the sign of GVs. For anisotropic behaviors of v_y with u_{yy} strain, the results are not similar. As seen in Fig. 5(d), the critical momenta $u_{yy} < 0$ emerge with maximum v_y and an increasing (decreasing) behavior appears before (after) these strains. On the other hand, both GVs of conduction bands show the same values at another critical strain $u_{yy} = -0.02$. In these cases, the maximum and converged values of v_y in the above-mentioned cases are the typical value of η_y.

One may also notice significant anisotropies in the EM for both the subbands. It is expected because of strong deviations in GV of these subbands. While m_y^* is much larger than m_x^* for both the lowest and highest branches of the conduction band in the absence of strain [see Fig. 3], in the presence of strain, the difference is by a few orders of magnitude. However as the strain increases this difference is reduced to only an order of magnitude. For example, for $u_{xx} = 0$, $u_{yy} = -0.04$ and $(+\sqrt{n^2+\delta^2}/\eta_x, 0)$, $1/m_x^*$ of both conduction branches is larger than its $1/m_y^*$ with a factor of 6 for $u_{yy} = 0$, $u_{xx} = 0.04$ and $(+\sqrt{n^2+\delta^2}/\eta_x, 0)$, whereas for a higher strain, $u_{xx} = u_{yy} = 0.1$, the ratio is around 1 for $(+\sqrt{n^2+\delta^2}/\eta_x, 0)$ point [See Fig. 6(a) and (b)]. Nevertheless, the same ratios are not maintained for other curves of Fig. 6(c) and (d). In other words, the momentum-dependent transport affects the anisotropy ratio as well. The rations above-mentioned are around 3 and 1, respectively, for low and high strains.

Theoretically, the positive and negative sign of EM refers to the concavity up and down of bands, respectively. Thus the band edge concavities have significant effects on the EMs and their signs. To understand the sign changes in Fig. 6(a) and (d), see Fig. 4(g) and (d), respectively. The blue and red bands show opposite concavities and different corresponding EM signs are expected to emerge. Fig. 6(a) and (d) show the detailed analysis performed for the above concavities. However, in all cases, strong anisotropy is evident.

The EMs are plotted as a function of strains to construct an identity of the critical strains. It is clear from Fig. 6(a) that the $1/m_x^*$ has two maxima (for the highest conduction band) and minima (for the lowest conduction band) values at $u_{xx} = +0.01$ and $+0.02$, while it is the same for both bands when $+\sqrt{n^2+\delta^2}/\eta_x < u_{xx} < -\sqrt{n^2+\delta^2}/\eta_x$. In other words, $1/m_x^*$ of the red conduction band increases with u_{xx} up to

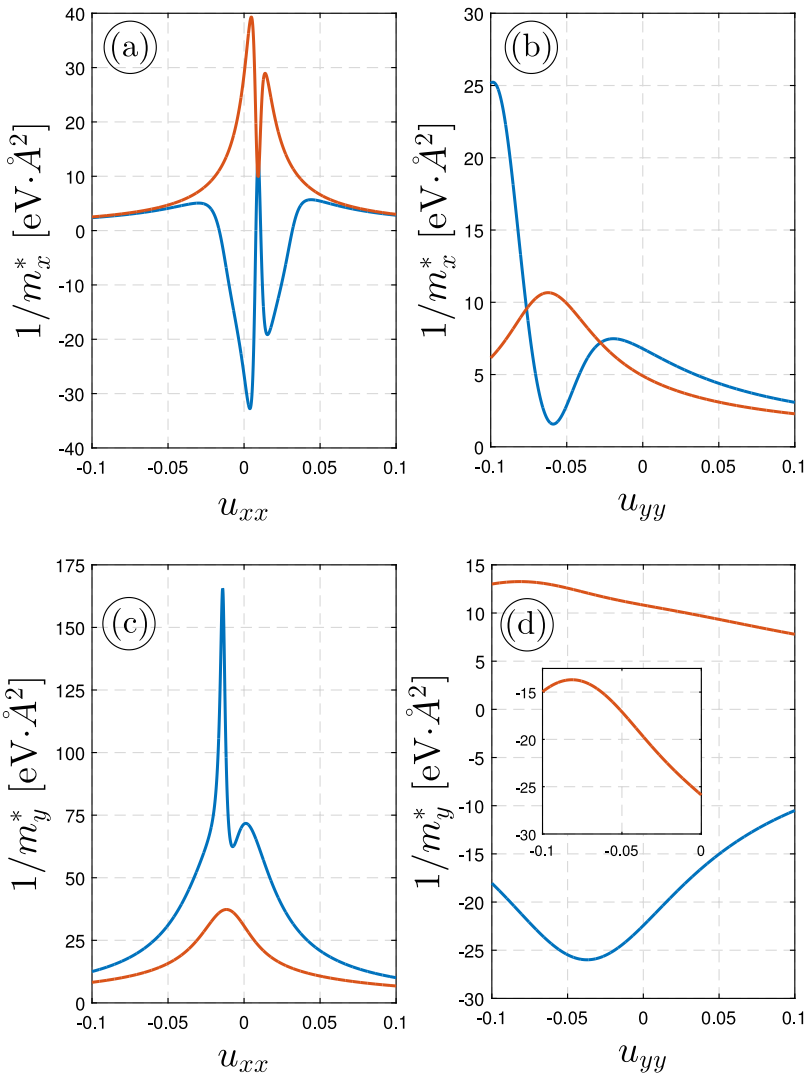

Fig. 6. Direction-dependent effective mass of Dirac fermions on the SnTe (001) surface for (a) $\{k_y = 0, k_x = +\sqrt{n^2+\delta^2}/\eta_x, u_{yy} = -0.04\}$, (b) $\{k_y = 0, k_x = +\sqrt{n^2+\delta^2}/\eta_x, u_{xx} = +0.04\}$ $k_x = 0$, (c) $\{k_x = 0, k_y = +n/\eta_y, u_{yy} = -0.04\}$, and (d) $\{k_x = 0, k_y = +n/\eta_y, u_{xx} = +0.04\}$. (For interpretation of the references to color in this figure legend, the reader is referred to the web version of this article.)

$u_{xx} = +0.01$, decreases up to $u_{xx} = +0.015$, increases up to $u_{xx} = +0.02$, and decreases for $u_{xx} > +0.02$. This is reversed for the blue conduction band. Also, both bands become the same at $u_{xx} = +0.015$. This is more noticeable in the case of $1/m_x^*$ as a function of u_{yy}. Note that there is still two critical $u_{yy} = -k_x - u_{xx}$ and $u_{yy} = -(n/\eta_y) + 3u_{xx}$ for which $1/m_x^*$ of red and blue bands demonstrates a peak, respectively, as illustrated in Fig. 6(b). Additionally, at $u_{yy} \simeq -k_x$, the blue band becomes minimum, i.e. $1/m_x^*$ of the blue band decreases with u_{yy} up to $u_{yy} \simeq -k_x$, increases up to $u_{yy} = -(n/\eta_y)+3u_{xx}$ and decreases forever for $u_{yy} > -(n/\eta_y)+3u_{xx}$, whereas $1/m_x^*$ of the red band increases with u_{yy} up to $u_{yy} = k_x$ and decreases for $u_{yy} > k_x$.

Briefly, the effect of the u_{xx} is to increase $1/m_y^*$ for both bands up to $u_{xx} = -0.02$, while is to decrease (oscillate) it for red (blue) conduction band when $u_{xx} > -0.02$, as shown in Fig. 6(c). Actually, $1/m_y^*$ decreases first for $-0.02 < u_{xx} < -0.01$, increases slightly for $-0.01 < u_{xx} < 0$ and decreases similar to the red band for $u_{xx} > 0$. Note, however, that this behavior is quite different for $1/m_y^*$ versus u_{yy}, as occurs in the simple case of an increase (decrease) up to $u_{yy} = -k_x - 2u_{xx}$ ($u_{yy} = -(n/\eta_y) + 2u_{xx}$) for the red (blue) band, while a decrease (increase) for $u_{yy} > -k_x - 2u_{xx}$ ($u_{yy} > -(n/\eta_y) + 2u_{xx}$), as represented in Fig. 6(d). The anisotropic EM is clear from the coefficients of the critical strains.

4. Summary

In summary, the significant effects of compressive and tensile strain on the GV and EM of the SnTe (001) surface Dirac fermions, as a TCI protected by the mirror symmetry, are investigated theoretically by applying the $\vec{k} \cdot \vec{p}$ theory. By deriving the pristine and strain-induced energy dispersion surface, the fermion GV and EM for SnTe (001) surface are obtained. Our results indicate that the band structure, GV and EM are strongly anisotropic. As strain increases, the surface does not display the mirror symmetry independent of the direction. We understood how to tune the GV and EM of SnTe (001) surface Dirac fermions for special purposes with the aid of strain. We emphasize that the GVs as well as EMs occurring in the results depend on both train modulus and direction. Furthermore, the difference in the evolution of heavy and light masses with strain contributes to improved both electronic and thermoelectric types of transport in this material.

CRediT authorship contribution statement

Nguyen T.T. Binh: Conceptualization, Investigation, Formal analysis, Software, Writing - review & editing. **Bui D. Hoi:** Investigation, Software, Formal analysis, Writing - review & editing. **Ho Viet:** Software, Formal analysis. **Tong S. Tien:** Investigation, Software, Formal

analysis. **Pham V. Dung:** Investigation, Software, Formal analysis. **Nguyen T. Dung:** Investigation, Software, Formal analysis. **P.T.T. Le:** Conceptualization, Methodology, Investigation, Formal analysis, Writing - review & editing.

Declaration of competing interest

The authors declare that they have no known competing financial interests or personal relationships that could have appeared to influence the work reported in this paper.

References

[1] B.A. Bernevig, T.L. Hughes, S.-C. Zhang, Science 314 (2006) 1757.
[2] M. König, S. Wiedmann, C. Brüne, A. Roth, H. Buhmann, L.W. Molenkamp, X.-L. Qi, S.-C. Zhang, Science 318 (2007) 766.
[3] M.Z. Hasan, C.L. Kane, Rev. Modern Phys. 82 (2010) 3045.
[4] X.-L. Qi, S.-C. Zhang, Rev. Modern Phys. 83 (2011) 1057.
[5] A. Bansil, H. Lin, T. Das, Rev. Modern Phys. 88 (2016) 021004.
[6] L. Fu, C.L. Kane, E.J. Mele, Phys. Rev. Lett. 98 (2007) 106803.
[7] D.J. Thouless, M. Kohmoto, M.P. Nightingale, M. den Nijs, Phys. Rev. Lett. 49 (1982) 405.
[8] S.-Y. Xu, Y. Xia, L.A. Wray, S. Jia, F. Meier, J.H. Dil, J. Osterwalder, B. Slomski, A. Bansil, H. Lin, R.J. Cava, M.Z. Hasan, Science 332 (2011) 560.
[9] M. Brahlek, N. Bansal, N. Koirala, S.-Y. Xu, M. Neupane, C. Liu, M.Z. Hasan, S. Oh, Phys. Rev. Lett. 109 (2012) 186403.
[10] S.-Y. Xu, C. Liu, N. Alidoust, M. Neupane, D. Qian, I. Belopolski, J.D. Denlinger, Y.J. Wang, H. Lin, L.A. Wray, G. Landolt, B. Slomski, J.H. Dil, A. Marcinkova, E. Morosan, Q. Gibson, R. Sankar, F.C. Chou, R.J. Cava, A. Bansil, M.Z. Hasan, Nature Commun. 3 (2012) 2191.
[11] J. Zhang, W.-X. Ji, C.-W. Zhang, P. Li, P.-J. Wang, Phys. Chem. Chem. Phys. 20 (2018) 24790.
[12] R.-W. Zhang, C.-W. Zhang, W.-X. Ji, S.-S. Li, S.-J. Hu, S.-S. Yan, P. Li, P.-J. Wang, F. Li, New J. Phys. 17 (2015) 083036.
[13] M. Yarmohammadi, Phys. Lett. A 380 (48) (2016) 4062.
[14] B.D. Hoi, M. Yarmohammadi, J. Magn. Magn. Mater. 454 (2018) 362.
[15] K.S. Novoselov, et al., Science 306 (5696) (2004) 666.
[16] M. Yarmohammadi, Chin. Phys. B 26 (2) (2017) 026502.
[17] A.H.C. Neto, F. Guinea, N.M.R. Peres, K.S. Novoselov, A.K. Geim, Rev. Modern Phys. 81 (1) (2009) 109.
[18] K.S. Novoselov, et al., Nature 438 (7065) (2005) 197.
[19] M. Yarmohammadi, J. Magn. Magn. Mater. 426 (2017) 621.
[20] M. Yarmohammadi, Phys. Lett. A 381 (14) (2017) 1261.
[21] M. Ezawa, Phys. Rev. Lett. 109 (5) (2012) 055502.
[22] M. Ezawa, New J. Phys. 14 (3) (2012) 033003.
[23] M. Yarmohammadi, RSC Adv. 7 (18) (2017) 10650.
[24] M. Yarmohammadi, Solid State Commun. 250 (2017) 84.
[25] A.P. Schnyder, S. Ryu, A. Furusaki, A.W.W. Ludwig, Phys. Rev. B 78 (2008) 195125.
[26] A. Kitaev, AIP Conf. Proc. 1134 (2009) 22.
[27] L. Fu, Phys. Rev. Lett. 106 (2011) 106802.
[28] S.-Y. Xu, C. Liu, N. Alidoust, M. Neupane, D. Qian, I. Belopolski, J. Denlinger, Y. Wang, H. Lin, L. Wray, G. Landolt, B. Slomski, J. Dil, A. Marcinkova, E. Morosan, Q. Gibson, R. Sankar, F. Chou, R. Cava, A. Bansil, M. Hasan, Nature Commun. 3 (2012) 1192.
[29] R.S.K. Mong, A.M. Essin, J.E. Moore, Phys. Rev. B 81 (2010) 245209.
[30] T.H. Hsieh, H. Lin, J. Liu, W. Duan, A. Bansil, L. Fu, Nature Commun. 3 (2012) 982.
[31] P. Dziawa, B.J. Kowalski, K. Dybko, R. Buczko, A. Szczerbakow, M. Szot, E. Łusakowska, T. Balasubramanian, B.M. Wojek, M.H. Berntsen, O. Tjernberg, T. Story, Nature Mater. 11 (2012) 1023.
[32] Y. Tanaka, Z. Ren, T. Sato, K. Nakayama, S. Souma, T. Takahashi, K. Segawa, Y. Ando, Nature Phys. 8 (2012) 800.
[33] Y. Ando, L. Fu, Annu. Rev. Condens. Matter Phys. 6 (2015) 361.
[34] J.C.Y. Teo, L. Fu, C.L. Kane, Phys. Rev. B 78 (2008) 045426.
[35] J. Liu, W. Duan, L. Fu, Phys. Rev. B 88 (2013) 241303(R).
[36] Y. Tanaka, T. Shoman, K. Nakayama, S. Souma, T. Sato, T. Takahashi, M. Novak, K. Segawa, Y. Ando, Phys. Rev. B 88 (2013) 235126.
[37] C.M. Polley, P. Dziawa, A. Reszka, A. Szczerbakow, R. Minikayev, J.Z. Domagala, S. Safaei, P. Kacman, R. Buczko, J. Adell, M.H. Berntsen, B.M. Wojek, O. Tjernberg, B.J. Kowalski, T. Story, T. Balasubramanian, Phys. Rev. B 89 (2014) 075317.
[38] R.-J. Slager, A. Mesaros, V. Juricic, J. Zaanen, Nature Phys. 9 (2012) 98.
[39] C.-K. Chiu, H. Yao, S. Ryu, Phys. Rev. B 88 (2013) 075142.
[40] T. Morimoto, A. Furusaki, Phys. Rev. B 88 (2013) 125129.
[41] P. Jadaun, D. Xiao, Q. Niu, S.K. Banerjee, Phys. Rev. B 88 (2013) 085110.
[42] W.A. Benalcazar, J.C.Y. Teo, T.L. Hughes, Phys. Rev. B 89 (2014) 224503.
[43] C. Fang, L. Fu, Phys. Rev. B 91 (2015) 161105(R).
[44] M. Diez, D.I. Pikulin, I.C. Fulga, J. Tworzydło, New J. Phys. 17 (2015) 043014.
[45] M. Kargarian, G.A. Fiete, Phys. Rev. Lett. 110 (2013) 156403.
[46] E.O. Wrasse, T.M. Schmidt, Nano Lett. 14 (2014) 5717.
[47] X. Zhou, C.-H. Hsu, T.-R. Chang, H.-J. Tien, Q. Ma, P.J. Herrero, N. Gedik, A. Bansil, V.M. Pereira, S.-Y. Xu, H. Lin, L. Fu, Phys. Rev. B 98 (2018) 241104(R).
[48] T. Morimoto, A. Furusaki, C. Mudry, Phys. Rev. B 91 (2015) 235111.
[49] P. Barone, D. Di Sante, S. Picozzi, Phys. Status Solidi RRL 7 (2013) 1102.
[50] L. Zhao, J. Wang, B.-L. Gu, W. Duan, Phys. Rev. B 91 (2015) 195320.
[51] Y. Tanaka, T. Sato, K. Nakayama, S. Souma, T. Takahashi, et al., Phys. Rev. B 87 (2015) 155105.
[52] M. Serbyn, L. Fu, Phys. Rev. B 90 (2014) 035402.
[53] E. Tang, L. Fu, Nature Phys. 10 (2014) 964.
[54] J. Liu, T.H. Hsieh, P. Wei, W. Duan, J. Moodera, et al., Nature Mater. 13 (2014) 178.
[55] X. Qian, L. Fu, J. Li, Nano Res. 8 (2015) 967.
[56] L. Fu, C.L. Kane, Phys. Rev. Lett. 109 (2012) 246605.
[57] O.I. Yuzephovich, M.Y. Mikhailov, S.V. Bengus, A.Y. Aladyshkin, E.E. Pestov, et al., Low Temp. Phys. 34 (2008) 985.
[58] P. Sessi, D. Di Sante, A. Szczerbakow, F. Glott, S. Wilfert, H. Schmidt, T. Bathon, P. Dziawa, M. Greiter, T. Neupert, G. Sangiovanni, T. Story, R. Thomale, M. Bode, Science 354 (2016) 1269.
[59] C. Fang, M.J. Gilbert, B.A. Bernevig, Phys. Rev. Lett. 112 (2012) 046801.
[60] Y. Okada, M. Serbyn, H. Lin, D. Walkup, W. Zhou, et al., Science 341 (2013) 1496.
[61] G.D. Mahan, Many Particle Physics, Plenum Press, New York, 1993.
[62] G. Grosso, G.P. Parravicini, Solid State Physics, Academic Press, New York, 2014.
[63] N.W. Aschcroft, Solid State Theory, Holt, Rinehart, and Wilson, 1976.
[64] K. Seeger, Semiconductor Physics, Springer-Verlag, 1985.
[65] C. Kittel, I, Wiley, second ed., 1986.
[66] W.A. Harrison, Solid State Theory, Dover, 1979.
[67] M. Yarmohammadi, K. Mirabbaszadeh, Phys. Chem. Chem. Phys. 21 (2019) 21633.
[68] M. Yarmohammadi, K. Mirabbaszadeh, J. Mater. Chem. A 7 (2019) 25573.
[69] D. Walkup, B.A. Assaf, K.L. Scipioni, R. Sankar, F. Chou, G. Chang, H. Lin, I. Zeljkovic, V. Madhavan, Nature Commun. 9 (2018) 1550.